Planetary and Space Science 194 (2020) 105115

Contents lists available at ScienceDirect

Planetary and Space Science

journal homepage: www.elsevier.com/locate/pss

The science mission of SpaceIL's Beresheet lander

Oded Aharonson [a,b,*], Christopher T. Russell [c], James W. Head III [d], Mark Wieczorek [e], Ian Garrick-Bethell [f,g], Benjamin P. Weiss [h], David E. Smith [h], Kathryn Rowe [c], Asaf Grosz [i], Shai Amrusi [i], Alexander Novoselsky [a], Nadav Nahaman [a], Yuval Grossman [a], Yonatan Shimoni [a], Ariel Gomez [j]

[a] Department of Earth and Planetary Sciences, Weizmann Institute of Science, Rehovot, Israel
[b] Planetary Science Institute, Tucson, AZ, USA
[c] Institute of Geophysics and Planetary Physics, University of California Los Angeles, Los Angeles, CA, USA
[d] Department of Earth, Environmental and Planetary Sciences, Brown University, Providence, RI, USA
[e] Observatoire de la Côte d'Azur, Nice, France
[f] Department of Earth and Planetary Sciences, University of California Santa Cruz, Santa Cruz, CA, USA
[g] School of Space Research, Kyung Hee University, Yongin-si, Gyeonggi-do, South Korea
[h] Department of Earth, Atmospheric and Planetary Sciences, Massachusetts Institute of Technology, Cambridge, MA, USA
[i] Department of Electrical and Computer Engineering, Ben-Gurion University, Be'er Sheva, Israel
[j] SpaceIL, Tel-Aviv, Israel

ARTICLE INFO

Keywords:
Moon
Lander
Magnetic field
Magnetometer

ABSTRACT

SpaceIL's lunar lander mission Beresheet was launched on February 22, 2019 and impacted its targeted landing site in Mare Serenitatis on the Moon on April 11, 2019. The spacecraft carried a package of scientific instruments including a fluxgate magnetometer and a retroreflector array for laser ranging, as well as a suite of cameras. Orbital measurements of the magnetic field from Kaguya and Lunar Prospector guided the selection of the landing site to a location west of Posidonius crater in the Serenitatis plains, where the magnitude of the modeled magnetic field reaches 8–10 nT at the surface. Data was collected by the SILMAG magnetometer from Earth orbit, lunar orbit, and during the descent maneuver, although its interpretation is hindered by the presence of a spacecraft field.

1. Introduction

SpaceIL's lunar lander mission named Beresheet (meaning 'in the beginning' or 'Genesis' in Hebrew) is the first Israeli mission beyond Earth orbit. SpaceIL is the organization established in 2011 originally to compete this mission in the Google Lunar XPRIZE (GLXP) competition, itself aimed at stimulating lunar exploration. The GLXP challenged non-governmental teams to land an unmanned robotic spacecraft on the Moon, travel 500 m, and transmit high-definition video and images back to Earth.

SpaceIL progressed to the final stages of the competition, which officially ended in March 2018 without a winner. However, SpaceIL had decided to complete the mission independent of the competition and an early 2019 launch date was set. The project was supported by the Israel Space Agency (ISA), the Israel Ministry of Science and Technology (IMOST), and the Israel erospace Industries (IAI), among others (Gibney, 2019).

The spacecraft was launched on February 22, 2019 onboard a SpaceX Falcon 9 vehicle from the Kennedy Space Center in Cape Canaveral, Florida. The mission consisted of three phases: multiple Earth orbits followed by lunar orbit insertion, a soft-landing maneuver, and stationary operation on the Moon's surface. Besides being the first Israeli spacecraft to leave Earth orbit, the mission included several science investigation goals which will be described below.

The main stages of mission timeline are outlined in Table 1 and shown in Fig. 1. Shyldkrot et al. (2019) outlines the trajectory, the maneuver strategy, and the navigation plan.

2. Scientific motivation

The primary scientific objective of the SpaceIL Beresheet mission was to measure regional and local magnetic field variations in order to improve our understanding of the Moon's current and past magnetic

* Corresponding author. Department of Earth and Planetary Sciences, Weizmann Institute of Science, 234 Herzl St., Rehovot, 7610001, Israel.
E-mail address: oded.aharonson@weizmann.ac.il (O. Aharonson).

https://doi.org/10.1016/j.pss.2020.105115
Received 28 July 2020; Received in revised form 4 October 2020; Accepted 6 October 2020
Available online 13 October 2020
0032-0633/

Table 1
Beresheet's mission timeline.

Date and Time, UTC	Event Description
Earth orbit	
22.02.2019 01:45	Launch from the Cape Canaveral Space Launch Complex 40 (SLC-40) by SpaceX Falcon 9
22.02.2019 02:18	Separation
24.02.2019 11:29–11:29	Apogee Maneuver (AM2): Elliptical orbit around Earth (apogee 70,000 km, perigee 650 km)
28.02.2019 19:29–19:33	Perigee Maneuver (PM1): orbit correction, Elliptical orbit around Earth (apogee 133,000 km, perigee 650 km)
07.03.2019 12:57–12:59	Perigee Maneuver (PM2): orbit correction, Elliptical orbit around Earth (apogee 270,000 km, perigee 1000 km)
19.03.2019 12:29–12:29	Perigee Maneuver (PM3): Elliptical orbit around Earth (apogee 430,000 km, perigee 1300 km)
20.03.2019 12:29–12:29	Orbital Plane Maneuver (OPM): orbit correction, Elliptical orbit around Earth (apogee 420,000 km, perigee 1300 km)
01.04.2019 05:59–06:00	Trajectory Correction Maneuver (TCM1): Elliptical orbit around Earth (apogee 430,000 km, perigee 2000 km)
Moon orbit	
04.04.2019 14:18–14:23	Lunar Orbit Insertion (LOI1): completion of lunar capture maneuver, entering elliptical orbit around the Moon (apocenter 10,246 km, pericenter 450 km)
07.04.2019 01:36–01:40	Lunar Orbit Insertion (LOI2): orbit correction, elliptical orbit around the Moon (apocenter 750 km, pericenter 470 km)
08.04.2019 04:48–04:48	Lunar Orbit Insertion (LOI2A): orbit correction, Elliptical orbit around the Moon (apocenter 750 km, pericenter 210 km)
09.04.2019 05:32–05:33	Lunar Orbit Insertion (LOI2B): orbit correction, Nearly circular orbit around the Moon (apocenter 210 km, pericenter 200 km)
Lunar landing	
10.04.2019 16:40–16:40	Descent Maneuver (DM1)
11.04.2019 19:23	Impact

environment. Measurements of magnetization of the lunar crust were planned from orbit, during landing and on the surface of the landing site. These objectives thus influenced the selection of the landing site.

The scientific payload of Beresheet lander is comprised of two instruments, whose installation positions on the spacecraft are shown in Fig. 2. The first is a SpaceIL fluxgate Magnetometer (SILMAG), provided by the University of California, Los Angeles. The second is the Laser Retroreflector Array (LRA), provided by NASA Goddard Space Flight Center (GSFC) (Fig. 3).

The LRA is a set of eight mirrors mounted into a dome-shaped aluminum frame (Sun et al., 2019), such that it reflects a laser beam back in the direction of its source. Specifically, LRA was designed such that reflections of pulses from a lidar such as the Lunar Orbiter Laser Altimeter (LOLA) would enable precise ranging between Beresheet and an orbiting spacecraft in the decades following the Beresheet landing.

In addition, six 8-megapixel CCD cameras (Imperx Bobcat B3320C) with Ruda optics and two sets of video processors for redundancy (5 panoramic cameras and a self-pointing camera) were integrated on the spacecraft, providing images intended for public engagement as well as scientific interpretation of the landing site.

3. The SpaceIL magnetometer

The SILMAG instrument was constructed using heritage designs from the Space Technology 5 (ST5) NASA mission (Strangeway et al., 2002; Russell et al., 2019). Further engineering assistance in calibration and testing was obtained from the Ben-Gurion University of the Negev. The fluxgate instrument design was selected due to its electronic simplicity, compact size, small weight, and low power consumption (Russell et al., 2016; Banfield et al., 2018). The instrument is a triaxial magnetometer with accuracy of 0.1 nT, digital resolution of 24 bits and dynamic range of $\pm 8\mu$T, designed to measure the magnetic field during cruise, landing, and on the surface of the Moon. Magnetometer data may be recorded at two sample rates: 10 Hz and 0.625 Hz, the latter representing 16-measurement averages of the former. The main SILMAG characteristics are presented in Table 2.

The instrument consists of two parts: an electronics unit and a sensor, connected by a harness (Fig. 4). The chassis of the electronics unit holds two electronics boards: a power board providing the necessary voltage levels and a signal board conditioning and digitizing the measurements.

Data in 24-bit, signed 2's complement format together with housekeeping information are output in asynchronous serial fashion via the RS-422 transceiver with fixed data rate of 10 Hz. The housekeeping data records the voltages and temperatures of the electronics in 16-bit, signed 2's complement format, with an addition of a time tag generated by the mission computer for synchronization of the data packets.

4. Landing site selection

In order to realize the mission goals, potential landing sites were identified satisfying both safety and scientific requirements of the mission. In the next subsections we will describe the engineering and science-driven requirements of the landing site and specify the relevant data products that were used. We will then outline the approach used in the selection of the final landing sites candidates.

4.1. Landing site requirements and constraints

A set of requirements were derived from engineering and science considerations, aimed to assure landing safety, communication, and science data acquisition. These fall in four categories: I. Descent, II. Touchdown, III. Surface operations, and IV. Science operations.

I. Descent
- I.a Navigation system precision requires a landing site of 15 km radius, centered on the optimal landing location. The spacecraft autonomous landing system dictates a landing ellipse with a semi-major axis of 15 km (along-track direction) and a smaller semi-minor axis. However, lack of sufficient knowledge on the approach trajectory at site selection time resulted in the circular region as defined.
- I.b Within the landing site defined above, topographic variations must not exceed 200 m peak-to-peak, for navigation performance.
- I.c The reflectance of the surface within the landing site defined above must be $\geq$0.11 at wavelengths 1550$\pm$20 nm, for laser range determination performance.
- I.d In addition to the primary landing site, two additional alternate sites are required within 4–15° in longitude West, and up to $\pm$4° in latitude away of the primary site, for which all requirements are satisfied.

II. Touchdown
- II.a Surface slopes must be $\leq$10° computed in the range of baselines 15–50 m, for lander stability.
- II.b A preference for surfaces exhibiting few craters 1–10 m in size.
- II.c Rock abundance must be $\leq$1.2% of the surface area for rocks greater than 10 cm in diameter, for lander leg safety.

III. Surface Operations
- III.a Landing site region must be within latitudes 30–60°N or 30–60°S, for lander thermal control during three Earth days of operations following landing.

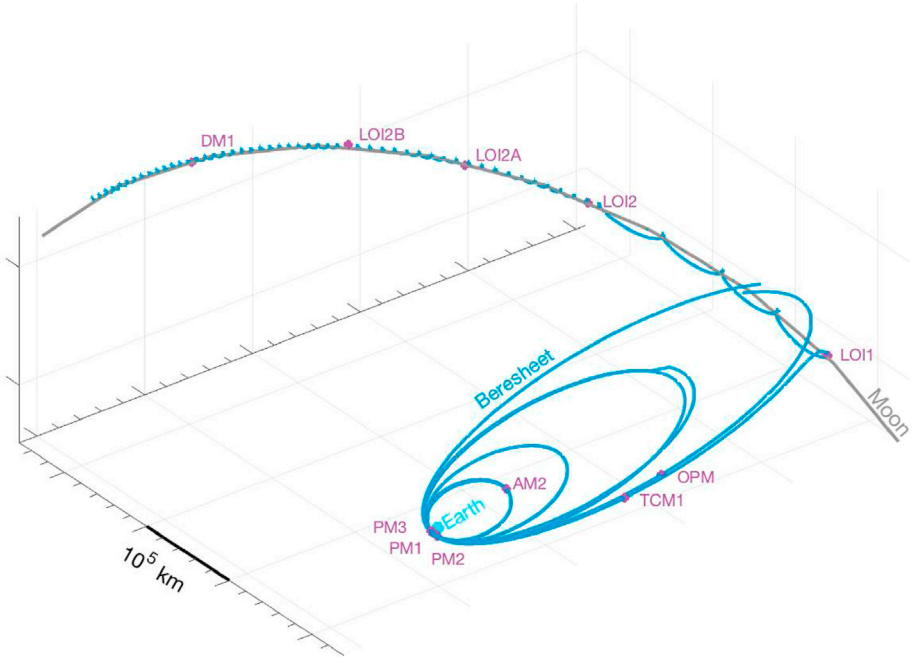

Fig. 1. Beresheet mission profile, shown in an Earth-centered inertial frame. Spacecraft maneuvers are indicated, starting at launch to the final descent maneuver in lunar orbit. Discontinuities in Beresheet's position are due to updates to the calculation of the orbital trajectory.

III.b Landing site must be within the geographic polygons shown in Fig. 5, for continuous Earth communication.

III.c The landing site was required to have unobstructed view in the direction of the Sun >3° in elevation and within ±30° in azimuth.

IV. Science Operations

IV.a The landing site must have a magnetic field magnitude ≥8.5 nT at the surface.

The requirements listed above guided the landing site candidates selection process. The final selection was made on the basis of human inspection of the available data, and in particular, high-resolution imagery.

4.2. Data sets

A quantitative analysis of the primary and alternate landing sites was performed to verify their compatibility with the mission constraints using data sets from various instruments.

Topography was based on the SELENE - LOLA Digital Elevation Model (SLDEM) by Barker et al. (2016) at a horizontal resolution of 512 pixel per degree (PPD) and typical vertical accuracy ~3–4 m. This product is available as a global map within the latitudes range 60°S-60°N and based on topographic heights acquired by LOLA, co-registered with set of global coverage DEM tiles produced by SELENE Terrain Camera.

Surface slopes and roughness, at 30–120 m baselines were taken from the Lunar Reconnaissance Orbiter (LRO) LOLA altimetry data (Smith et al., 2010; Rosenburg et al., 2011). The slope map comprised of a bi-directional slope calculated from a plane fit of 5–15 topographic points acquired by LOLA. Roughness values measured as the topographic variance, were taken as the root mean square (RMS) of altitudes in reference to that plane. Both slope and roughness are averaged to produce gridded maps at 16 PPD. LOLA data were similarly used for the surface slopes estimation on a 60 m baseline for the Luna-25 mission landing sites in the South Polar region of the Moon (Djachkova et al., 2017).

To estimate the abundance of exposed surface rocks above 0.1 m, we used the LRO Diviner Radiometer rock abundance (RA) map (Bandfield et al., 2011). These data give the areal fraction of the surface covered by rock fragments by modeling the surface temperature variations with a two component mixture of high and low thermal inertia. The variations are sensitive to rocks on the scale estimated to be ~0.5 m. To extrapolate to smaller rock sizes we use a power law size-frequency distribution with an exponent based on fitting the particle size distribution of Shoemaker and Morris (1970) derived from imaging at the Surveyor landing sites. Thus, the rock abundance derived from Diviner data D_0 was extrapolated from the assumed Diviner scale $D_0 = 0.5$ m to a scale D, using

$$\mathrm{RA}(D) = \mathrm{RA}_0 (D/D_0)^{\gamma+2} \quad (1)$$

with $\gamma = -2.56$, which is the best fit between the two data sets for Surveyor 3 mission. This data was sampled at 128 PPD between latitudes 80°N-80°S.

Surface reflectance at the wavelength of the laser range finder of the spacecraft was extracted from the data acquired by the SELENE Multi-band Imager near-infrared instrument, in the 1548 nm channel (Ohtake et al., 2008). This product is available in tiles of 1 × 1° containing reflectance in 9 channels at original resolution of 2048 PPD. For our survey, we extracted the relevant single wavelength data and rebinned the data at a resolution of 512 PPD.

We used crater counts published previously by Schultz et al. (1977) for Mare Serenitatis, and by Hiesinger et al. (2000) for more extensive mare units.

To estimate slopes and surface roughness at meter-scales, we used images acquired by the LRO Narrow Angle Camera (LROC NAC). These are panchromatic images with resolution 0.5 m/pixel (Robinson et al., 2010), from which areas with low concentration of visible boulders were identified.

Stereo pairs of LROC NAC images were used to produce local Digital Elevation Models (Kokhanov et al., 2018). While no suitable pairs were found within the landing ellipse, we used pairs from adjacent areas in Mare Serenitatis with the same geological formations and appearance in images to produced DEMs at the resolution of 2 m/pixel using SOCET SET (Tran et al., 2010). From these, slopes on short scales were studied. We also compared the results to the DEMs from Kaguya Terrain Camera with a resolution of 4096 PPD (~7 m/pix at the equator), but these showed greater random and systematic errors on small scales.

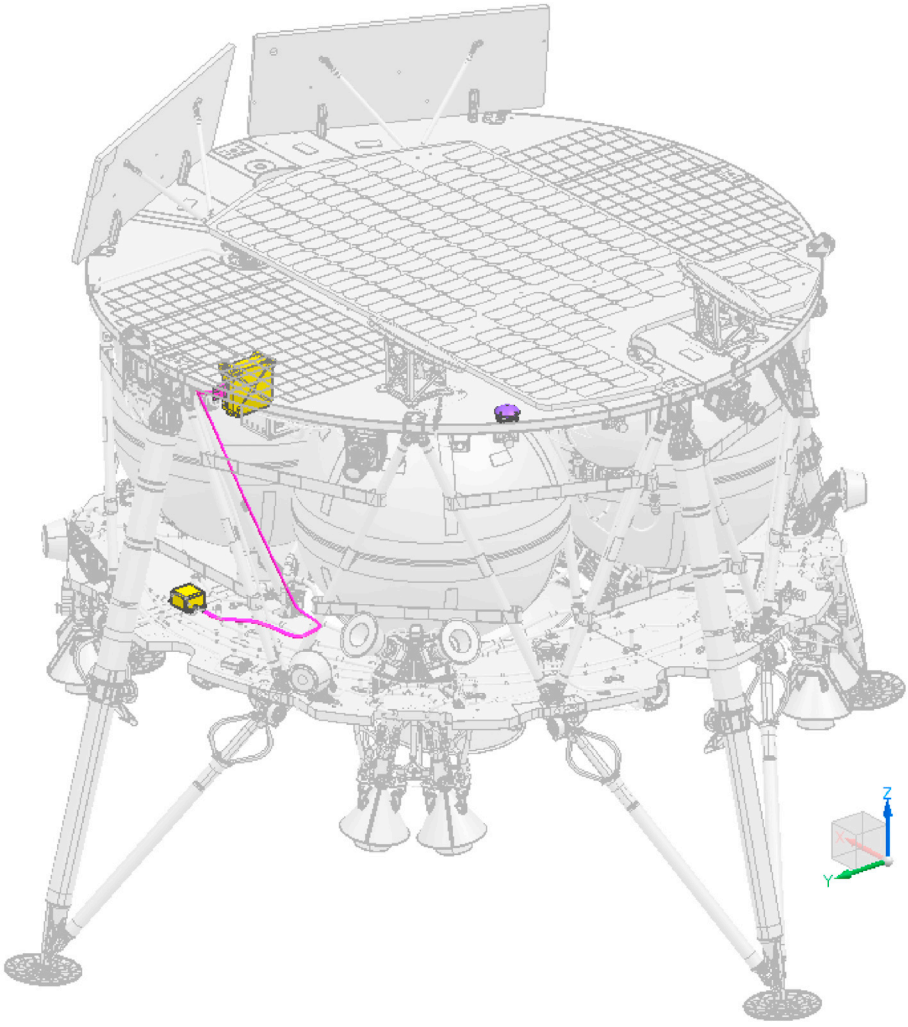

Fig. 2. Perspective view of the Beresheet spacecraft, highlighting the science payload. The SILMAG magnetometer sensor mounted on the lower deck and electronics unit mounted below the upper deck (yellow) are connected by the harness (magenta). The LRA is mounted on the top of the upper deck (purple). The spacecraft body-fixed coordinate system is also indicated. For scale, the lander measures 1.5 m in height. (For interpretation of the references to color in this figure legend, the reader is referred to the Web version of this article.)

Fig. 3. The Laser Retroreflector Array (LRA). The unit is 50 mm in diameter at the base and 16 mm in height. Photo credit: SpaceIL/Xiaoli Sun/GSFC.

To characterize principal geological and mineralogical units within the proposed landing site, we performed an analysis using geologic maps (Carr, 1966; Scott, 1972) and the Moon Mineralogy Mapper (M^3) data set (Kaur et al., 2013).

Finally, the lunar crust magnetization magnitude was estimated from magnetic field measurements acquired from orbit by the Kaguya Lunar Magnetometer and Lunar Prospector Magnetometers. The model in Tsunakawa et al. (2015) uses these data acquired at high altitude and provides extrapolated values for the surface field (albeit at lower resolution than we seek to measure).

4.3. Selected landing sites

The selection of landing sites was performed in two stages: first, global filtering to a set of few potential areas, and second, detailed analysis of selected areas.

Global filtering was performed following the constraints enumerated above (Sec. 4.1), and using the data sets previously described (Sec 4.2). The general approach was to produce binary maps at a resolution of 16 PPD encoding each criterion. Regions of radius 15 km were then mapped in which >95% of the area was verified to meet all criteria.

While initial landing sites surveys yielded candidate landing sites in both the northern and southern hemispheres (Grossman et al., 2017), application of the full set of engineering constraints and consideration of the multi-scale properties of the surface restricted the sites to areas within the lunar maria. Detailed analysis of selected areas was performed using relief information on the scale of the spacecraft from stereo imagery. The final primary landing site that was selected is located in the northeastern portion of Mare Serenitatis, approximately 120 km south of the northern boundary of the mare and 220 km west of the 95 km

Table 2
Summary SILMAG instrument characteristics.

Parameter	Value	Unit
Physical specifications		
Dimensions of electronics unit	105.4 x 109.2 x 60.6	mm
Dimensions of sensor	70.1 x 53.8 x 32.1	mm
Length of harness	1050	mm
Mass of electronics unit	390	g
Mass of sensor	160	g
Mass of harness	49	g
Sensor thermal limits (operating)	[-100,80]	°C
Sensor thermal limits (survival)	[-130,120]	°C
Electronics thermal limits (operating)	[-30,65]	°C
Electronics thermal limits (survival)	[-50,95]	°C
Pressure range	[10^{-10},760]	Torr
Electrical specifications		
Supply voltage	28	Vdc
Power consumption	1–2	W
Measurement specifications		
Sample rate	10	Hz
Digital resolution (each axes)	24	bit
Accuracy (each axes)	0.1	nT
Dynamic range (X,Y,Z)	±8690,±8250,±8450	nT
Offset @ 24 °C (X,Y,Z)	11.6, 8.0, −1.1	nT
Noise density at 1 Hz (X,Y,Z)	0.05, 0.04, 0.1	nT/$\sqrt{\text{Hz}}$
Sensor temperature field offset (X,Y,Z)	0.05, 0.06,0.12	nT/°C
Sensor temperature field gain (X,Y,Z)	0.2, 0.4, 0.5	% over 100 °C
Electronics temperature field offset (X,Y,Z)	0.04, 0.03, 0.06	nT/°C
Electronics temperature field gain (X,Y,Z)	0.2, 0.14, 0.18	% over 100 °C

diameter Posidonius crater (Fig. 6). Centered on 33.190°N, 19.395°E, the provisionally named 'Posidonius I' site is flanked by two backup sites, 'Posidonius II' (center coordinates – 31.968°N, 18.296°E) and 'Posidonius III' (center coordinates – 32.609°N, 17.507°E). Assessment of these sites indicates a relative paucity of craters and other hazards. It does exhibit a measurable magnetic anomaly from orbit that meets the science goals of the mission stated above.

Table 3 summarizes the results of each criterion from our geomorphic analysis of the primary and alternate landing ellipses. For robustness against outliers, maximum and minimum values presented correspond to 97.5 and 2.5 percentiles of the data, respectively. For comparison, we also show values of the same set of criteria as computed for the Apollo 11 landing site.

The final landing ellipse is located within Mare unit S13 (Hiesinger et al., 2000). Using the absolute model age (AMA) by Neukum (1983), the age for this unit is $3.49^{+0.08}_{-0.05}$ Ga (Hiesinger et al., 2000). In order to refine the AMA of the sequence of basalt plains while maintaining adequate counting statistics, we subdivided this unit into three sub-units showing consistent geomorphological and spectral properties: S13_1, S13_2, and S13_3 (marked in red, blue, and black, Fig. 7a).

The AMA analysis was performed using the software Craterstats 2.0, with results outlined in Fig. 7b. For the sub-unit S13_1, which shows similar properties to those of the final landing ellipse, we obtained an AMA of $2.59^{+0.12}_{-0.13}$ Ga, indicating the flows in this region are younger than previously thought. This is also consistent with the relatively low number of craters within the landing area, a characteristic that was used in the site selection. For sub-unit S13_2 we obtained an intermediate age of $3.41^{+0.052}_{-0.077}$ Ga, and for S13_3 we obtained $3.48^{+0.085}_{-0.190}$ Ga. We note this latter unit exhibits a

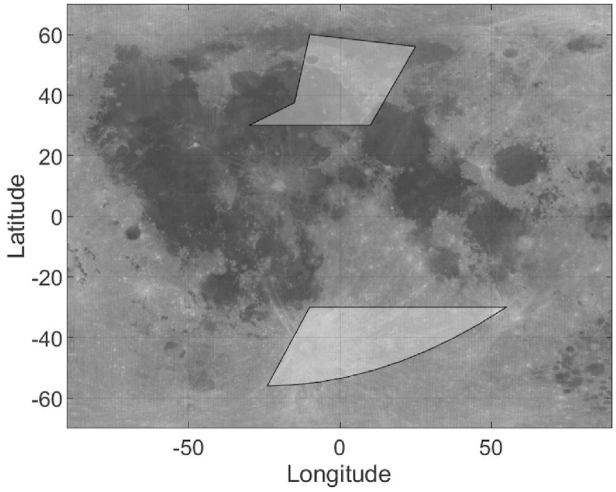

Fig. 5. Lunar nearside map showing landing site limitation (white polygons) for Earth communication in post-landing operations.

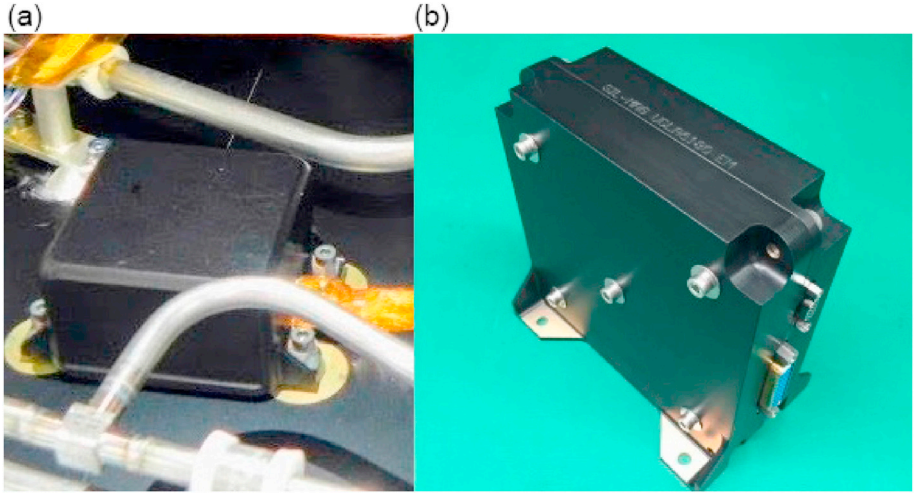

Fig. 4. The SpaceIL Magnetometer (SILMAG): sensor mounted on the spacecraft bottom deck (a) and electronics unit (b). The sensor dimensions are 70.1 x 53.8 × 32.1 mm and the electronic box are 105.4 x 109.3 × 60.5 mm.

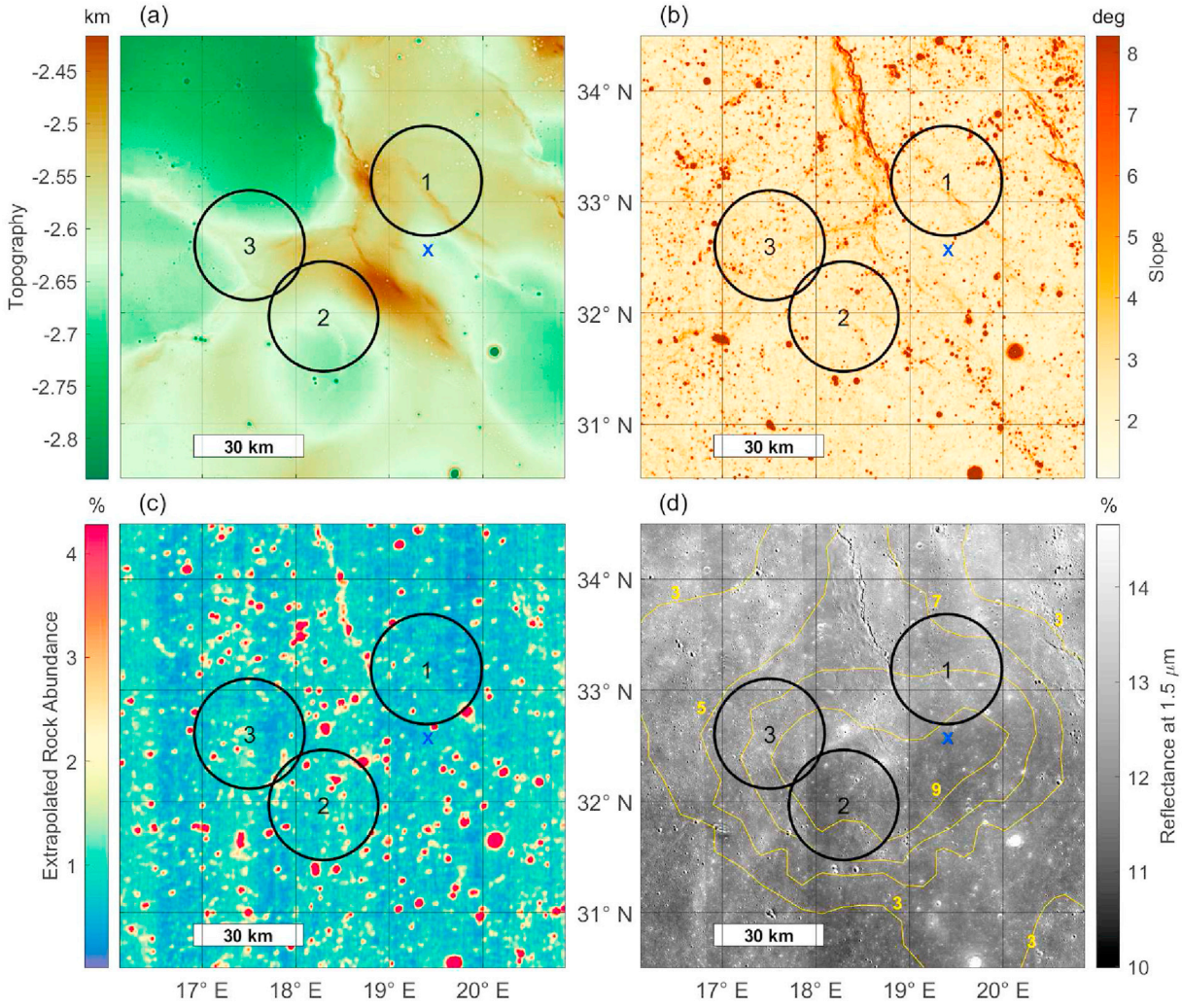

Fig. 6. Topography (a), surface slopes (b), extrapolated rock abundance at 10 cm scale (c), and reflectance at 1.5 μm wavelength (d) of the planned Beresheet landing sites in Mare Serenitatis, near Posidonius crater. Black circles indicate the landing sites selected. The actual impact location is indicated by a blue 'x'. Yellow contours indicate the value of the surface magnetic field extrapolated from orbital measurements of Tsunakawa et al. (2015). (For interpretation of the references to color in this figure legend, the reader is referred to the Web version of this article.)

Table 3
Summary of results for criteria analyzed for the Beresheet spacecraft's landing ellipse at Posidonius I, its adjacent sites, Posidonius II and III, and Apollo 11 landing site for comparison. Slope and roughness values were computed on a 60 m baseline.

Parameter	Requirement	Posidonius I	Posidonius II	Posidonius III	Apollo 11
Longitude [°E]		19.395	18.296	17.507	23.473
Latitude [°N]		33.190	31.968	32.609	0.674
Topographic range [m]	<200	95	192	163	308
Rock abundance [%]	<1.2	0.73	1.05	0.87	1.01
Max. slope [°]	<5	4.13	3.77	3.99	7.23
Max roughness [m]		1.22	1.11	1.25	1.27
Mean roughness [m]		0.88	0.75	0.89	0.85
Min reflectance	>0.11	0.121	0.112	0.117	0.088
Surface magnetic field [nT]	>8.5	8.92	10.59	9.92	6.08

distinct population of craters in small size range, indicating an additional younger age estimate due to resurfacing of older Mare basalts.

Fig. 8 shows the impact site of Beresheet, as imaged by LROC NAC. Following the landing attempt on 11.4.2019, efforts were undertaken by the LRO team to locate the crash site using LOLA reflections from the LRA, or with imagery. With no confirmation of the physical state and orientation of the LRA on the surface, the LOLA search did not produce any unambiguous pulse return identifications. LROC successfully imaged the presumed crash site 11 days following the impact, and indeed found a feature that was not present in previous images at the location 32.5956°N, 19.3496°E (coordinates defined as in LRO Project (2008)). The center of the feature is dark, several meters wide, and is interpreted as the roughening of the surface due to the direct impact. A larger surrounding region extending typically 10's m with a ray directed southwest

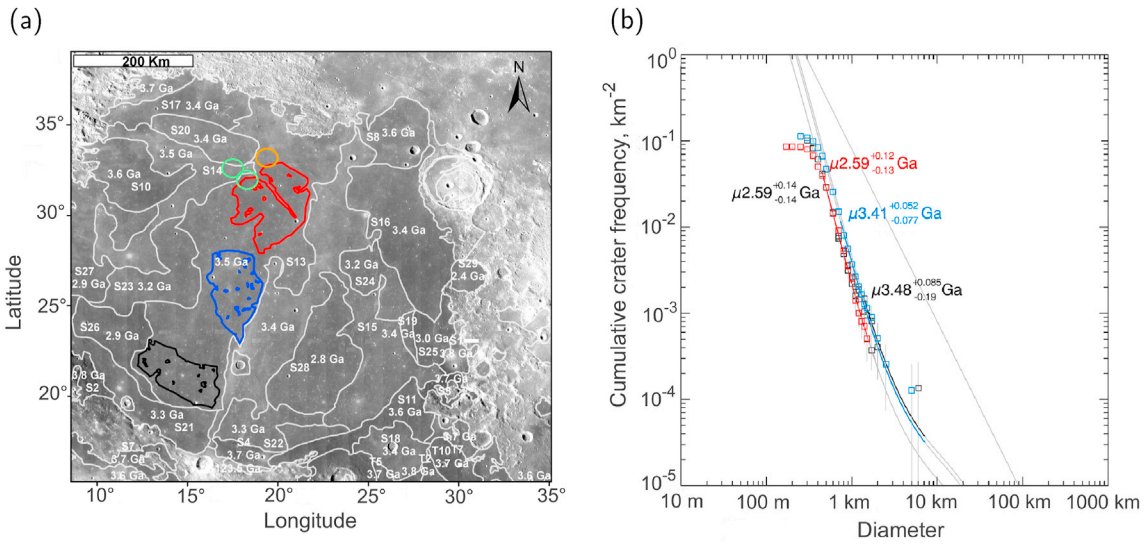

Fig. 7. (a) The crater measurement map of Mare Serenitatis with Mare age units by Hiesinger et al. (2000). Shown is the LRO Wide Angle Camera 100 m/pixel mosaic basemap with the three subunits S13_1, S13_2, and S13_3 (marked in red, blue and black) we defined within Mare unit S13. The final landing ellipse (orange) and two backup ellipses (light green) are also noted. (b) Derived crater size-frequency distribution with absolute model age (AMA) of the defined subunits with corresponding colors. (For interpretation of the references to color in this figure legend, the reader is referred to the Web version of this article.)

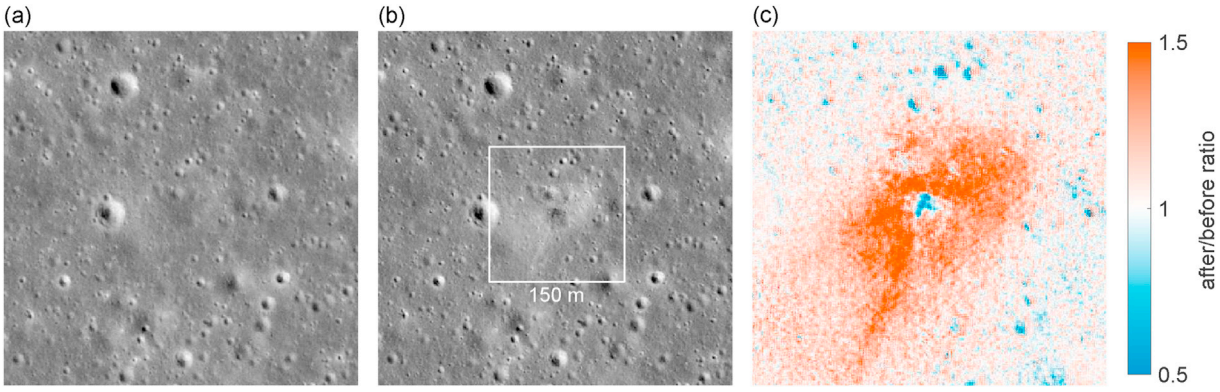

Fig. 8. LROC NAC images showing the Beresheet impact site. (a) LROC image M1236487095L acquired on 16.12.2016, pre-impact, frame is 400 m wide. (b) LROC image M1310536929R acquired on 22.4.2019, post-impact, frame is 400 m wide. (c) A ratio image of the after/before images, focusing on the impact site. The frame is 150 m wide, and shows a lowering of the reflectance with an area within ~5 m of the impact location, with a brightening over a larger area reaching 100 m from the site. Image credit: NASA/GSFC/ASU.

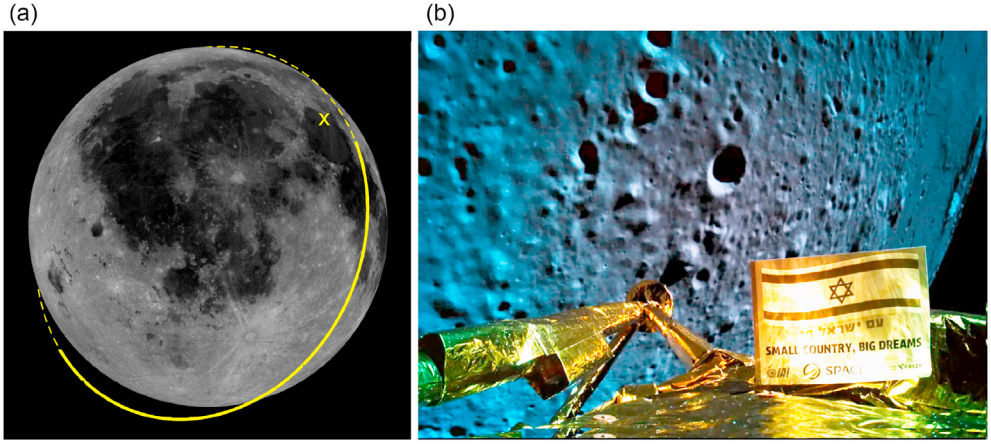

Fig. 9. (a) The position of the final orbit of the Beresheet spacecraft around the Moon (dashed) as well as an interval during which SILMAG measurements were obtained and downlinked (solid). The impact point is also indicated (x). (b) An image captured by Beresheet's camera during the final orbit before the landing attempt. One of the lander legs and plaque are visible in the foreground, with the lunar surface in the background. The image has been enhanced and does not represent true colors. Image credit: SpaceIL/IAI. (For interpretation of the references to color in this figure legend, the reader is referred to the Web version of this article.)

> 100 m long shows a higher albedo. This is interpreted as resulting from the redistribution of fine dust on and smoothing of the surface due to rapid motion of gas/particles away from the impact site.

5. SILMAG results

The SpaceIL Magnetometer (SILMAG) was turned on and acquired data several times during near-Earth orbit, cruise, lunar orbit, and descent maneuver. Fig. 9a shows the nominal position of the final orbit around the Moon, as well as the location of the spacecraft impact point on the surface. A time interval during which SILMAG data were acquired and downlinked is indicated (data was likely acquired all the way to surface, but no further downlinks containing science data occurred). These measurements, as well as the calibration data that were acquired in Earth orbit, show that the instrument responded to variations in the environmental field in space (Aharonson et al., 2020). However, our analysis indicates that the signal was dominated by the spacecraft field, which likely exceeded the designed dynamic range of the sensor in one axis. In this field regime, laboratory tests verify the SILMAG control electronics allow detection of field variations as seen in the data, but the value of the field reported cannot be reliably interpreted.

The calibration measurements performed in the spacecraft integration facility during tests did not show this effect. This is likely due to the combination of our externally applied field, Earth's magnetic field, and its induced component on the spacecraft counteracted the spacecraft remnant field, allowing correct measurements to be acquired within the instrument's dynamic range. Separating the aforementioned components proved to be difficult with an installation within the spacecraft volume, lacking separation typically afforded by a boom. We conclude that a magnetometer installation within the spacecraft volume, while in principle possible, hinders the interpretation of measurements in space. Prelaunch calibration measurements allow only partial representation of the spacecraft field in the space environment.

During the spacecraft's final descent maneuver, a fault indication from one of the two Inertial Measurements Units (IMU) and an attempt to command a power-on of this unit led to the mission computer reset, main thruster shutdown, an uncontrolled, low angle (<10°), high-speed impact on the lunar surface, and communication loss (Shyldkrot et al., 2019). An image acquired during the final orbit, just prior to the landing maneuver at altitude ~22 km, is shown in Fig. 9b.

Although we did not have the opportunity to obtain magnetic measurements from an altitude in which the lunar field would be discerned from that due to the spacecraft, our best indications are that the instrument performed well and according to design throughout the mission.

Author statement

None.

Declaration of competing interest

The authors declare that they have no known competing financial interests or personal relationships that could have appeared to influence the work reported in this paper.

Acknowledgments

This project was supported by the Helen Kimmel Center for Planetary Science, the Minerva Center for Life Under Extreme Planetary Conditions, by the I-CORE Program of the PBC and ISF (Center #1829/12) and the Israeli Ministry of Science (#3–13592). We would like to thank Prof. Dr. H. Heisinger for assistance with crater dating and Yunan Yu for her work on data processing. IGB acknowledges support from the BK21 plus program of the National Research Foundation (NRF) of the Republic of Korea. OA would like to particularly thank the Adolf and Mary Mil Foundation for their generous support.

References

Aharonson, O., Russell III, C.T., H, J.W., Wieczorek, M., Garrick-Bethell, I., Weiss, B.P., Smith, D.E., Rowe, K., Gomez, A., Grosz, A., Amrusi, S., Novoselsky, A., Nahaman, N., Grossman, Y., Shimoni, Y., 2020. The science mission of SpaceIL's Beresheet lander: plans and results. Lunar Planet. Sci. 51 abst. #1267.

Bandfield, J.L., Ghent, R.R., Vasavada, A.R., Paige, D.A., Lawrence, S.J., Robinson, M.S., Dec 2011. Lunar surface rock abundance and regolith fines temperatures derived from LRO Diviner Radiometer data. J. Geophys. Res. Planets 116 (E12), E00H02.

Banfield, D., Rodriguez-Manfredi, J.A., Russell, C.T., Rowe, K.M., Leneman, D., Lai, H.R., Cruce, P.R., Means, J.D., Johnson, C.L., Mittelholz, A., Joy, S.P., Chi, P.J., Mikellides, I.G., Carpenter, S., Navarro, S., Sebastian, E., Gomez-Elvira, J., Torres, J., Mora, L., Peinado, V., Lepinette, A., , The TWINS Team, Hurst, K., Lognonné, P., Smrekar, S.E., Banerdt, W.B., Dec 2018. InSight auxiliary payload sensor suite (APSS). Space Sci. Rev. 215 (1), 4.

Barker, M., Mazarico, E., Neumann, G., Zuber, M., Haruyama, J., Smith, D., 2016. A new lunar digital elevation model from the Lunar Orbiter Laser Altimeter and SELENE terrain camera. Icarus 273, 346–355.

Carr, M.H., 1966. Geologic map of the mare Serenitatis region of the moon. In: Geologic Atlas of the Moon. U.S. Geological Survey.

Djachkova, M.V., Litvak, M.L., Mitrofanov, I.G., Sanin, A.B., May, 2017. Selection of Luna-25 landing sites in the South polar region of the Moon. Sol. Syst. Res. 51 (3), 185–195.

Gibney, E., 2019. First private moon lander heralds new lunar space race. Nature 566, 434–436.

Grossman, Y., Aharonson, O., Novoselsky, A., 2017. Landing site selection for the SpaceIL mission to the Moon. Lunar Planet. Sci. 48 abst. #1914.

Hiesinger, H., Jaumann, R., Neukum, G., Head III, J.W., 2000. Ages of mare basalts on the lunar nearside. J. Geophys. Res. Planets 105 (E12), 29239–29275.

Kaur, P., Bhattacharya, S., Chauhan, P., Ajai Kumar, A.K., 2013. Mineralogy of mare Serenitatis on the near side of the moon based on chandrayaan-1 moon Mineralogy mapper (M^3) observations. Icarus 222 (1), 137–148.

Kokhanov, A., Karachevtseva, I., Zubarev, A., Patraty, V., Rodionova, Z., Oberst, J., 2018. Mapping of potential lunar landing areas using LRO and SELENE data. Planet. Space Sci. 162, 179–189.

LRO Project, 2008. A standardized lunar coordinate system for the Lunar Reconnaissance Orbiter. LRO Project White Paper, version 4. URL. http://lunar.gsfc.nasa.gov/library/451-SCI-000958.pdf.

Neukum, G., 1983. Meteoriten bombardement und datierung planetarer oberflächen. Habilitation dissertation for faculty membership. Ludwig-Maximilians University München.

Ohtake, M., Haruyama, J., Matsunaga, T., Yokota, Y., Morota, T., Honda, C., LISM team, 2008. Performance and scientific objectives of the SELENE (Kaguya) Multiband imager. Earth Planets Space 60 (4), 257–264.

Robinson, M., Brylow, S., Tschimmel, M., et al., 2010. Lunar reconnaissance orbiter camera (LROC) instrument overview. Space Sci. Rev. 150 (1–4), 81–124.

Rosenburg, M.A., Aharonson, O., Head, J.W., Kreslavsky, M.A., Mazarico, E., Neumann, G.A., Smith, D.E., Torrence, M.H., Zuber, M.T., 2011. Global surface slopes and roughness of the moon from the lunar orbiter laser altimeter. J. Geophys. Res. Planets 116 (E2), E02001.

Russell, C.T., Anderson, B.J., Baumjohann, W., Bromund, K.R., Dearborn, D., Fischer, D., Le, G., Leinweber, H.K., Leneman, D., Magnes, W., Means, J.D., Moldwin, M.B., Nakamura, R., Pierce, D., Plaschke, F., Rowe, K.M., Slavin, J.A., Strangeway, R.J., Torbert, R., Hagen, C., Jernej, I., Valavanoglou, A., Richter, I., Mar, 2016. The magnetospheric multiscale magnetometers. Space Sci. Rev. 199 (1), 189–256.

Russell, C.T., Rowe, K.M., Joy, S.P., Aharonson, O., Amrusi, S., Grosz, A.G., Wieczorek, M., Weiss, B.P., Head, J.W., Garrick-Bethell, I., 2019. SILMAG: a fluxgate magnetometer on board the SpaceIL lunar lander. Lunar Planet. Sci. 50 abst. #1728.

Schultz, P.H., Greeley, R., Gault, D.E., 1977. Interpreting statistics of small lunar craters. Lunar Planet. Sci. 8 abst. #1295.

Scott, D.H., 1972. Geologic map of the eudoxus quadrangle of the moon. In: Geologic Atlas of the Moon. U.S. Geological Survey.

Shoemaker, E.M., Morris, E.C., 1970. Physical characteristics of the lunar regolith determined from Surveyor television observations. Radio Sci. 5 (2), 129–155.

Shyldkrot, H., Shmidt, E., Geron, D., Kronenfeld, J., Loucks, M., Carrico, J., Policastri, L., Taylor, J., 08, 2019. The first commercial lunar lander mission: Beresheet. In: AAS/AIAA Astrodynamics Specialist Conf, pp. 1–13.

Smith, D., Zuber, M., Jackson, G., et al., 2010. The lunar orbiter laser altimeter investigation on the lunar reconnaissance orbiter mission. Space Sci. Rev. 150 (1), 209–241.

Strangeway, R.J., Russell, C.T., Moldwin, M.B., Slavin, J.A., Le, G., May, 2002. Fluxgate magnetometers for space Technology 5. In: AGU Spring Meeting. GP51A–09.

Sun, X., Smith, D.E., Hoffman, E.D., Wake, S.W., Cremons, D.R., Mazarico, E., Lauenstein, J.-M., Zuber, M.T., Aaron, E.C., 2019. Small and lightweight laser retroreflector arrays for lunar landers. Appl. Optic. 58 (33), 9259–9266.

Tran, T., Howington-Kraus, E., Archinal, B., Rosiek, M., Lawrence, S.J., Gengl, H., Nelson, D., Robinson, M.S., Beyer, R., Li, R., Oberst, J., Mattson, S., LROC Science Team, 2010. Generating digital terrain models from LROC stereo images with SOCET SET. Lunar Planet. Sci. 41 abst. #2515.

Tsunakawa, H., Takahashi, F., Shimizu, H., Shibuya, H., Matsushima, M., 2015. Surface vector mapping of magnetic anomalies over the moon using Kaguya and Lunar Prospector observations. J. Geophys. Res. Planets 120 (6), 1160–1185.